frontiers in Materials

ORIGINAL RESEARCH
published: 03 January 2017
doi: 10.3389/fmats.2016.00058

# Transparent Oxyfluoride Nano-Glass Ceramics Doped with $Pr^{3+}$ and $Pr^{3+}$–$Yb^{3+}$ for NIR Emission

*Giulio Gorni[1], Alessandro Cosci[2,3], Stefano Pelli[2,3], Laura Pascual[4], Alicia Durán[1] and M. J. Pascual[1]**

[1] Instituto de Cerámica y Vidrio, Consejo Superior de Investigaciones Científicas (CSIC), Madrid, Spain, [2] Microdevices for Photonics Laboratory (MIP-LAB), Istituto di Fisica Applicata "Nello Carrara", Consiglio Nazionale delle Ricerche (CNR), Sesto Fiorentino, Italy, [3] Museo Storico della Fisica e Centro Studi e Ricerche Enrico Fermi, Roma, Italy, [4] Instituto de Catálisis y Petroleoquímica, Consejo Superior de Investigaciones Científicas (CSIC), Madrid, Spain

$Pr^{3+}$–$Yb^{3+}$ co-doped oxyfluoride glasses and glass-ceramics (GCs) containing $LaF_3$ nanocrystals have been prepared to obtain NIR emission of $Yb^{3+}$ ions upon $Pr^{3+}$ excitation in the blue region of the visible spectrum. Two different compositions have been tested: 0.1–0.5 Pr–Yb and 0.5–1 Pr–Yb, in addition to $Pr^{3+}$ singly doped samples. The crystallization mechanism of the nano-GCs was studied by differential thermal analysis revealing that it occurs from a constant number of nuclei, the crystal growth being limited by diffusion. High-resolution transmission microscopy demonstrated that phase separation acts as precursor for $LaF_3$ crystallization and a detailed analysis of the chemical composition (EDXS) revealed the enrichment in $RE^{3+}$ ions inside the initial phase separated droplets, from which the $LaF_3$ crystals are formed. The $RE^{3+}$ ions incorporation inside $LaF_3$ crystals was also proved by photoluminescence measurements showing Stark splitting of the $RE^{3+}$ ions energy levels in the glass-ceramic samples. Lifetime measurements showed the existence of a better energy transfer process between $Pr^{3+}$ and $Yb^{3+}$ ions in the GCs compared to the as made glass. The highest value of energy transfer efficiency is 59% and the highest theoretical quantum efficiency is 159%, obtained for GCs 0.1–0.5 Pr–Yb treated at 620°C for 40 h.

**Keywords: transparent, glass-ceramics, rare-earths, crystallization, down-conversion, solar energy**

OPEN ACCESS

***Edited by:***
*Joachim Deubener, Clausthal University of Technology, Germany*

***Reviewed by:***
*Paul M. Voyles, University of Wisconsin-Madison, USA*
*Chao Liu, Wuhan University of Technology, China*

****Correspondence:***
*Maria Jesús Pascual*
*mpascual@icv.csic.es*

***Specialty section:***
*This article was submitted to Glass Science, a section of the journal Frontiers in Materials*

***Received:*** *27 May 2016*
***Accepted:*** *14 December 2016*
***Published:*** *03 January 2017*

***Citation:***
*Gorni G, Cosci A, Pelli S, Pascual L, Durán A and Pascual MJ (2017) Transparent Oxyfluoride Nano-Glass Ceramics Doped with Pr3+ and Pr3+–Yb3+ for NIR Emission. Front. Mater. 3:58. doi: 10.3389/fmats.2016.00058*

## INTRODUCTION

Solar green energy is one of the emerging fields where rare earth (RE) ions are intensively used to improve silicon solar cells (SSCs) efficiency. In fact, the most important routes to reduce costs and promote the use of solar energy are: decrease refining and crystallization cost of silicon (the most widely used semiconductor), to use less silicon (thinner cells), developing thin films solar cells of less expensive materials (organic, polymeric) and/or improving SSCs efficiency.

Currently, many efforts are focused in the modification of the photovoltaic (PV) cells to make them more efficient. The main problem to improve PV energy conversion efficiency is associated with the spectral mismatch between the energy distribution of photons in the incident solar spectrum and the band-gap of silicon (Huang et al., 2013). Therefore, in the last years, solar down-converter materials doped with RE ions, able to convert the blue part of the solar spectrum to the range 980–1050 nm,

where silicon presents the best response, are becoming increasingly important (Trupe et al., 2002; Richards, 2006; van der Ende et al., 2009).

According to Abrams et al. (2011), a theoretical improvement of SSCs could be as high as 7% for an ideal lossless system; however, improvements (even though smaller than 7%) could be reached with a properly engineered solar converter layer.

Among the converter materials, glasses and glass-ceramics (GCs) for PV application are increasingly important thanks to their relatively easy production and engineering and their capability of hosting a great variety of RE ions in different concentrations.

Oxyfluoride nano-GCs containing luminescent RE ions have been extensively studied for their good mechanical and optical properties. Oxyfluoride nano-GCs are very attractive host materials, because they combine the very low phonon energy of fluoride nano-crystals environment, especially $LaF_3$ (<450 $cm^{-1}$). They are able to host $Ln^{3+}$ ions giving rise to high quantum efficiencies, with the high chemical and mechanical stability of a silicate glass matrix (de Pablos-Martín et al., 2012).

This paper describes the structural and optical properties of $LaF_3$ containing GCs doped with $Pr^{3+}$ and $Pr^{3+}$–$Yb^{3+}$ of composition $55SiO_2$–$20Al_2O_3$–$15Na_2O$–$10LaF_3$ (mol%) produced by melting-quenching (MQ). The properties of the un-doped glass system have been extensively studied elsewhere (Bhattacharyya et al., 2009; Hemono et al., 2009; de Pablos-Martín et al., 2011).

There are many published examples of different glass systems and crystalline phases studied for solar application with $Pr^{3+}$–$Yb^{3+}$. Indeed, we have chosen doping concentrations also relying on literature.

Chen et al. (2008) studied β-$YF_3$ containing GCs doped with 0.1 $Pr^{3+}$ and 0.1–1.5 $Yb^{3+}$ (mol %), obtaining the highest $Yb^{3+}$ emission for 1.0 $Yb^{3+}$ while for 1.5 $Yb^{3+}$ a quenching effect was observed. The corresponding energy transfer efficiency (ETE) and quantum efficiency (QE) were 90 and 190%, respectively.

Lakshminarayana and Qiu (2009) studied Pr–Yb down-conversion (DC) in oxyfluoride germanate glasses made by MQ and doped with 0.5 $Pr^{3+}$ and 2–30 $Yb^{3+}$ (mol %). The highest DC signal at 980 nm was measured for the 0.5 $Pr^{3+}$–4 $Yb^{3+}$ but the 0.5 $Pr^{3+}$–2 $Yb^{3+}$ produced almost as good results. $Pr^{3+}$ lifetimes at 608 nm were 9.5 and 4.9 μs and the ETE 35 and 66% for 2 and 4$Yb^{3+}$, respectively.

Chen et al. (2012) and Zhou et al. (2012) characterized oxyfluoride GCs containing $CaF_2$ nanocrystals. Chen et al. (2012) prepared materials with composition $45SiO_2$–$25Al_2O_3$–$10Na_2O$–$20CaF_2$–$0.1PrF_3$–$y YbF_3$ ($y = 0.1$–$1.0$) (mol%). The NIR emission suffered quenching for 1 $Yb^{3+}$ and the most intense signal was obtained for 0.5$Yb^{3+}$. The decay curve of $Pr^{3+}$:$^3P_0$–$^3H_6$ at 610 nm was measured and the lifetime for 0.5 $Yb^{3+}$ was 78 μs, and the ETE and QE were 53 and 153%, respectively. Zhou et al. (2012) studied the compositions $60SiO_2$–$20Al_2O_3$–$20CaF_2$:$0.4Pr^{3+}$/$x Yb^{3+}$ ($x = 0$, 1, 2, and 4) (mol%). For $Yb^{3+}$ concentrations higher than 1 mol% a quenching of $Yb^{3+}$ emission at 980 nm was measured and for 1 $Yb^{3+}$ the QE was 158%. The authors also tested a c-Si solar cell covered by the doped samples and measured a decrease compared with that covered by a host glass. Their conclusion was that a more efficient solar cell could be obtained by a proper ion doping concentration, an optimized sample thickness and the introduction of an antireflection film on the interface air-glass interface as well as the introduction of a waveguide structure on the DC layer to reduce emission losses.

Katayama studied the DC process of Pr–Yb in oxyfluoride glasses (Katayama and Tanabe, 2010a,b) and in $SrF_2$ GCs [Katayama and Tanabe, 2010a,b (p. 2); Katayama and Tanabe, 2013] with variable $Yb^{3+}$ concentration: 0.1 $Pr^{3+}$–$x Yb^{3+}$ ($x = 0$–2.9) obtaining the best DC emission for the highest $Yb^{3+}$ concentration. The ETE from the $Pr^{3+}$:$^3P_0$ to $Yb^{3+}$:$^2F_{5/2}$ increases from 42% for the glass to 75% for GCs, and the main ET process is a two-step process with $Yb^{3+}$ and $Pr^{3+}$ emission at 980 and 1300 nm, respectively. $Pr^{3+}$ emission at 1300 nm was more quenched, due to phonons, than in $SrF_2$-containing GCs.

Gao and Wondraczek (2013) obtained DC in boro-aluminosilicate glasses and $LaBO_3$ GCs doped with 1 $Pr^{3+}$–$x Yb^{3+}$ ($x = 0.1$–5). The best DC signal at 980 nm was obtained for 0.5 $Yb^{3+}$, the signal being quenched for higher concentrations, and the maximum value of the QE, obtained for 5 $Yb^{3+}$, was 183%.

Among all the studied materials there are a few examples regarding $LaF_3$-containing GCs doped with RE for DC produced by MQ, from which we point out the work of Xu et al. (2011) dealing with oxyfluoride GCs doped with $Pr^{3+}$–$Yb^{3+}$ of composition $40SiO_2$–$30Al_2O_3$–$18Na_2O$–$12LaF_3$ (mol%). However, in the work of Xu, the most relevant conclusions are as follows: (1) $Pr^{3+}$ ions are preferentially incorporated inside $LaF_3$ crystals, as shown by the increase of $Pr^{3+}$ emission at 600 nm in GCs compared to glass and (2) on the contrary $Yb^{3+}$ ions are not hosted inside $LaF_3$; therefore, the precipitation of $LaF_3$ crystals cannot improve the ET between $Pr^{3+}$ and $Yb^{3+}$.

Another study of $LaF_3$ crystals for DC emission is due to Deng et al. (2011) who studied crystalline powders of $LaF_3$ doped with $Pr^{3+}$–$Yb^{3+}$ prepared by co-precipitation method using $La^{3+}$, $Pr^{3+}$, and $Yb^{3+}$ as nitrates and $NH_4HF_2$ as fluorine source. For a fixed $Pr^{3+}$ concentration of 0.5 mol% several $Yb^{3+}$ concentrations were tested. With the increase of $Yb^{3+}$ concentration the visible emission from $Pr^{3+}$ weakens monotonically, while the NIR emission of $Yb^{3+}$ intensifies. However, a decrease of the $Yb^{3+}$ emission occurs for concentrations higher than 3%.

Xiang et al. (2014) studied $Pr^{3+}$–$Yb^{3+}$ doped β-$NaLuF_4$ hexagonal nanoplates with a size of 250 nm × 110 nm, synthesized by a solvo-thermal process. The ET from $Pr^{3+}$ ions to $Yb^{3+}$ ions occurs only by a two-step ET process when the $Yb^{3+}$ concentration is very low; however, increasing the $Yb^{3+}$ concentration, a cooperative ET process occurs for $Yb^{3+}$ concentration as high as 20 mol%.

Furthermore, there are many publications about spectroscopic characterization of RE ions doped materials for DC, but very few papers exist where a correlation between optical properties and material processing is made.

In this paper, glasses and GCs of composition $55SiO_2$–$20Al_2O_3$–$15Na_2O$–$10LaF_3$ (mol%) doped with 0.1 $Pr^{3+}$, 0.5 $Pr^{3+}$, 0.1–0.5 $Pr^{3+}$–$Yb^{3+}$, and 0.5–1 $Pr^{3+}$–$Yb^{3+}$ have been prepared. The structural properties of the materials have been studied by differential thermal analysis (DTA), X-ray diffraction (XRD), TEM and the optical properties by UV–VIS Absorption, photoluminescence (PL), and lifetime decay. The differences of the DC properties of the samples are described and the relationship of material processing with the optical properties is given.

# MATERIALS AND METHODS

## Glass Melting and Crystallization

Oxyfluoride glasses with composition $55SiO_2$–$20Al_2O_3$–$15Na_2O$–$10LaF_3$ (mol%) (55Si–10La) have been prepared by melting reagent grade $SiO_2$ sand (Saint-Gobain, Aviles, Spain, 99.6%), $Al_2O_3$ (Panreac), $Na_2CO_3$ (Sigma-Aldrich, >99.5%), $LaF_3$ (Alfa Aesar, 99.99%). $Pr^{3+}$ and $Yb^{3+}$ were added as fluorides (Alfa Aesar, 99.99%) in 0.1–0.5 and 0.5–1 concentrations (mol%). Samples doped with only $Pr^{3+}$ were also prepared for comparison of the optical properties. A more complete description of glass preparation was given in (de Pablos-Martín et al., 2011).

$Al_2O_3$ was previously annealed at 800°C for 12 h. Batch materials were weighed to obtain 100 g of glass, mixed for 1 h to ensure a good homogenization, put in a covered Pt crucible and annealed for 2 h at 1200°C. The Pt crucible was then placed in an elevator furnace for 1.5 h at 1650°C, the molten glasses were quenched in air onto a brass mold, fused again for 30 min to improve homogeneity and quenched onto a cold (−10°C) brass mold. The glasses were annealed at 600°C for 30 min for stress relaxation.

Glass-ceramics were obtained by heat treatment at 620°C for 1, 3, 5, 20, 40, and 80 h and at 660 and 680°C for 20 h. In all the cases, a heating rate of 10°C/min was used followed by quenching in air.

Heat treatments were performed on bulk specimens (size 1–1.25 mm).

## DTA and Crystallization Mechanism

Non-isothermal crystallization kinetics was studied by DTA/TG (SDT Q600—TA Instruments). Measurements have been performed on 20–30 mg of glass with particles size between 1 and 1.25 mm to reproduce bulk conditions. DTA scans were carried out with heating rates in the range 10–60°C/min.

The glass transition temperature $T_g$, crystallization activation energy $E_a$, and Avrami parameters ($n$, $m$) were calculated from DTA measurements.

The Avrami parameter $n$ allows assessing the crystallization process and was obtained employing the Ozawa equation (Ozawa, 1970):

$$\left(\frac{d\left[\ln\left[-\ln(1-x)\right]\right]}{d(\ln q)}\right)_T = -n, \tag{1}$$

where $x$ is the partial area of the crystallization peak calculated for a fixed temperature $T$ and $q$ is the heating rate. By using the Kissinger equation (Kissinger, 1956) the crystallization activation energy $E_a$ was obtained by

$$\ln\left(\frac{q}{T_p^2}\right) = -\frac{E_a}{RT_p} + C, \tag{2}$$

where $T_p$, $R$, and $C$ are the crystallization peak temperature, the gas constant and a constant, respectively. Finally, the $m$ parameter, representing the growth dimensionality, was obtained by the Matusita equation (Matusita and Sakka, 1980):

$$\ln\left(\frac{q^n}{T_p^2}\right) = -\frac{mE_a}{RT_p} + C'. \tag{3}$$

## X-Ray Diffraction

The heat-treated samples were milled and sieved (< 63 μm) and characterized by XRD with a Bruker D8 Advance diffractometer. Diffractograms were acquired in the rage $10 \leq 2\theta \leq 70°$ with a step size of 0.02° and 1 s acquisition for each step. Crystals size, $D$, was estimated using the Scherrer equation (Eq. 4), where $\lambda$ is the wavelength (1.54056 Å—$CuK\alpha_1$), $B_m$ the full width at half maximum of the $LaF_3$ peak (111) and θ its diffraction angle. The factor 0.94 corresponds to spherical crystals. Pseudo-Voigt function has been used to fit diffraction peak parameters. The instrumental broadening $B_i$ has been also taken into account using NaF powder properly milled and sieved (<63 μm):

$$D = \frac{0.94\lambda}{\cos\theta\sqrt{B_m^2 - B_i^2}}. \tag{4}$$

Crystalline growth can be described by the following equation:

$$r = Ut^p, \tag{5}$$

where $r$ is the crystal radius, $U$ the crystal growth rate, $t$ the time, and $p$ a growth exponent. The logarithmic form of Eq. 5 is commonly used:

$$\log(r) = \log(U) + p\log(t). \tag{6}$$

## High-Resolution Transmission Microscopy (HRTEM)

TEM samples of glasses and GCs were prepared by cutting slices, plane parallel grinding, dimpling to a residual thickness of 10–15 μm, and ion-beam thinning using $Ar^+$ ions. The angle of incidence was set to 8°, the beam energy to 5 kV, current to 5 mA, and milling time to 10–14 h. HRTEM including scanning transmission microscopy-high angle annular dark field and energy dispersive X-ray spectroscopy (EDXS) were performed with a JEOL 2100 field emission gun transmission electron microscope operating at 200 kV and providing a point resolution of 0.19 nm. The microscope was equipped with an energy dispersive X-ray spectrometer (EDXS—INCA x-sight, Oxford Instruments). EDXS analysis was performed in STEM mode, with a probe size of *ca*. 1 nm. In order to determine the particle distribution, we first assumed the particles to be spheres. No high contrast was obtained when working in the Scherzer focus, the shape of the particles was not well defined and difficult to measure. Thus, slightly under-focused TEM images were used to solve this problem. HAADF-STEM images were obtained where the particle shape was more distinguishable, and it is possible to measure the average diameter of the particles. By this method, only well-defined particles were measured which still resulted in a statistically well-representative data collection.

## Optical Properties

Bulk specimens were cut from the annealed glass and heat treated to obtain glass-ceramic materials. 0.1 Pr and 0.1–0.5 Pr–Yb glasses were treated at 620°C for 20 h and 40 h, and at 660°C for 20 h. 0.5 Pr and 0.5–1 Pr–Yb glasses were treated at 620°C for 40 h and 660°C for 20 h. All the samples have been

polished and optically characterized by UV–VIS absorption and PL spectroscopy.

UV–VIS spectra (Lambda 950—Perkin Elmer) were acquired between 300–2200 nm.

A photomultiplier tube (PMT) R6872 for UV–VIS and a Peltier cooled PbS for NIR detection were used as detectors.

A lock-in (5210-Princeton Research Instrument) configuration with an InGaN led at 435 nm (Roithner) as source for $Pr^{3+}$ excitation and a fiber laser at 976 nm to excite $Yb^{3+}$ ions was used to obtain PL spectra. A 2 × 2 $mm^2$ spot was produced with a lens focusing system and the samples were excited on the side edge to reduce re-absorption processes. Emission spectra were collected by an iHR-320 (Jobin-Yvon) spectrometer equipped with two gratings: 1200 g/mm blazed at 500 nm, and 600 g/mm blazed at 1000 nm. The detection system was calibrated using an incandescence lamp with known emission spectrum. A S-20 PMT and an InGaAs PD were used for UV–VIS and IR detection, respectively. Finally, all PL spectra were properly corrected for the instrument response.

Lifetime decay curves, upon excitation at 435 nm, were acquired with a fast oscilloscope (Tektronix), and the source was modulated electronically by a controller (ITC4000-Thorlabs).

For no single exponential decay, lifetimes were calculated using the following formula:

$$\tau_{avg} = \frac{\int_0^\infty t\, I(t)dt}{\int_0^\infty I(t)dt}. \quad (7)$$

The ETE and the QE were calculated using the following equations:

$$ETE = 1 - \frac{\tau_{Pr/Yb}}{\tau_{Pr}}, \quad (8)$$

$$QE = \eta_{Pr}(1 - ETE) + 2\eta_{Yb}ETE, \quad (9)$$

where $\tau_{Pr}$ and $\tau_{Pr/Yb}$ are the $Pr^{3+}$ lifetime, corresponding to the same excited state level, in doped and co-doped samples, while $\eta_{Pr}$ and $\eta_{Yb}$ are the $Pr^{3+}$ and $Yb^{3+}$ QEs.

# RESULTS AND DISCUSSION

## DTA and Crystallization Mechanism

Differential thermal analysis curves and the variation of glass transition temperature ($T_g$), crystallization starting temperature ($T_x$), and crystallization peak temperature ($T_p$), with the heating rate are given in **Figures 1A,B** for the samples doped with 0.1–0.5 Pr–Yb.

It was not possible to estimate $T_g$, $T_x$, $T_p$ from DTA curves performed at heating rate of 10°C/min due to very small endothermic peak ($T_g$) and exothermic peak ($T_x$, $T_p$) corresponding to $LaF_3$ crystallization. For 0.5–1 Pr–Yb doped glass the first values were obtained from a heating rate of 30°C/min.

The stability parameter, defined as $\Delta T = T_p - T_g$, is 114°C for both co-doped glasses for a heating rate of 10°C/min (calculated by extrapolation from the fits). The variation of $T_x$ and $T_p$ with the heating rate is faster than that of $T_g$, as confirmed by the slope parameter α in the equation $T = \alpha q$, summarized in **Table 1**. The calculated $T_g$ for a heating rate of 10°C/min are 570°C for 0.1–0.5 Pr–Yb and 585°C for 0.5–1 Pr–Yb. Higher $T_x$ and $T_p$

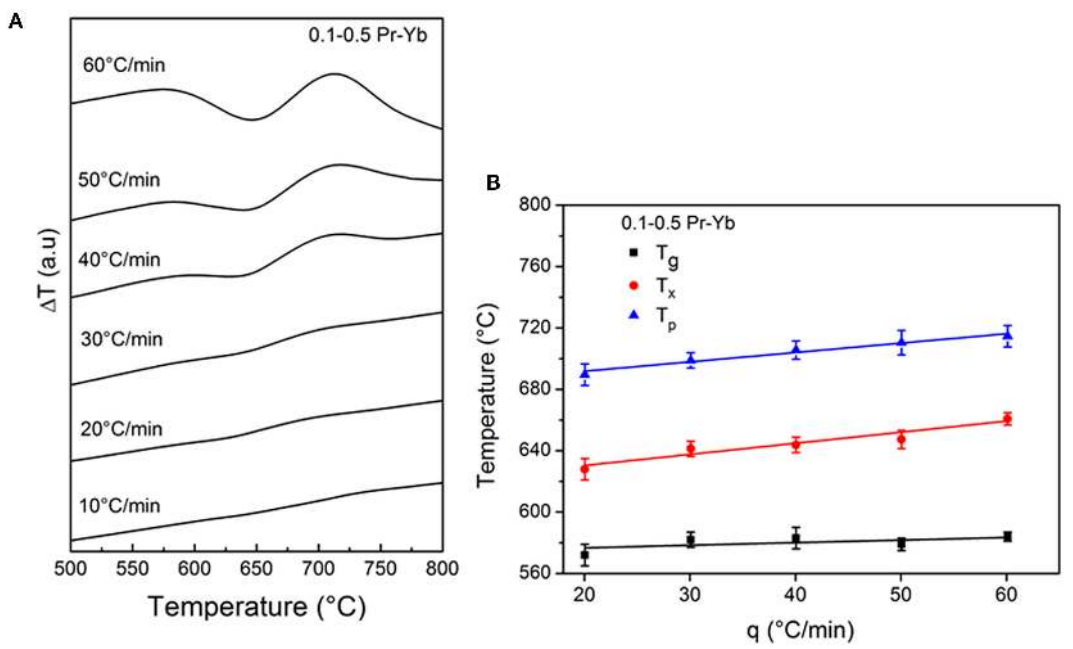


**FIGURE 1** | **(A)** Differential thermal analysis curves for 0.1–0.5 Pr–Yb glass performed at heating rates 10–60°C/min. **(B)** Variation of the glass transition temperature (square), crystallization starting temperature (circle), and $LaF_3$ crystallization peak temperature (triangle) with the heating rate.

values indicate a delay of the crystallization onset for materials with higher concentration of dopants.

By using Eq. 2, crystallization activation energies were calculated and their values are (329 ± 16) kJ/mol and (342 ± 18) kJ/mol for 0.1–0.5 Pr–Yb and 0.5–1 Pr–Yb, respectively. These results are similar to those obtained for the un-doped (de Pablos-Martín et al., 2011) and $Tm^{3+}$ doped glass (de Pablos-Martín et al., 2013), Avrami *n* parameter was calculated, using Eq. 1, from the slope of each line; a *n* mean value was obtained from the slope of the five lines represented in **Figures 2A,B** for 0.1–0.5 Pr–Yb and 0.5–1 Pr–Yb, respectively. By substituting the calculated crystallization activation energy into the Matusita equation (Eq. 3) and plotting the left side of Eq. 3 as a function of $E_a/RT_p$, the *m* parameter has been obtained from the slope of the lines represented in **Figures 2C,D**.

For 0.1–0.5 Pr–Yb, $n = 1.23 \pm 0.08$ and $m = 1.2 \pm 0.1$, while for 0.5–1 Pr–Yb $n = 0.86 \pm 0.08$ and $m = 0.84 \pm 0.08$. The two values of (*n, m*) for each composition are the same within uncertainties. The higher value obtained for the 0.1–0.5 Pr–Yb glass could be interpreted considering that the crystallization process is faster than for the 0.5–1 Pr–Yb glass. These parameters can be approximated to the nearest integer or semi-odd integer resulting in $n = 1$ and $m = 1$ for both materials. This means that the use of Kissinger equation is valid for the calculation of the crystallization activation energy and corresponds to a volumetric crystallization with crystal growth controlled by diffusion (Donald, 2004). The same (*n, m*) parameters were also obtained for the un-doped glass and for $Tm^{3+}$ doped glass (de Pablos-Martín et al., 2013), confirming that dopants do not affect the crystallization mechanism but may affect the crystallization kinetics and influence $LaF_3$ crystals size.

**TABLE 1 | Coefficients α (min) from the lines $T = \alpha$, *q* for the glass transition temperature ($T_g$), crystallization starting temperature ($T_x$), and crystallization peak temperature ($T_p$).**

| Glass | $\alpha_g$ | $\alpha_x$ | $\alpha_p$ |
|---|---|---|---|
| 55Si–10La 0.1–0.5 Pr–Yb | 0.17 ± 0.02 | 0.7 ± 0.1 | 0.61 ± 0.06 |
| 55Si–10La 0.5–1 Pr–Yb | 0.46 ± 0.07 | 0.7 ± 0.1 | 0.54 ± 0.06 |

## X-Ray Diffraction

X-ray diffraction measurements for GCs 0.1–0.5 Pr–Yb treated at 620°C for 1, 3, 5, 20, 40, and 80 h are given in **Figure 3A**, while diffractograms for heat treatment at 620, 660, and 680°C for 20 h are compared in **Figure 3B**. Very similar diffractograms have been obtained for GCs 0.5–1 Pr–Yb and are not represented.

In all the cases, $LaF_3$ was the only appearing crystalline phase confirmed by the reference (JCPDS 32-0483). All the distinguishable peaks of the diffraction pattern were labeled by Miller indexes. Crystals size was estimated using the generalized

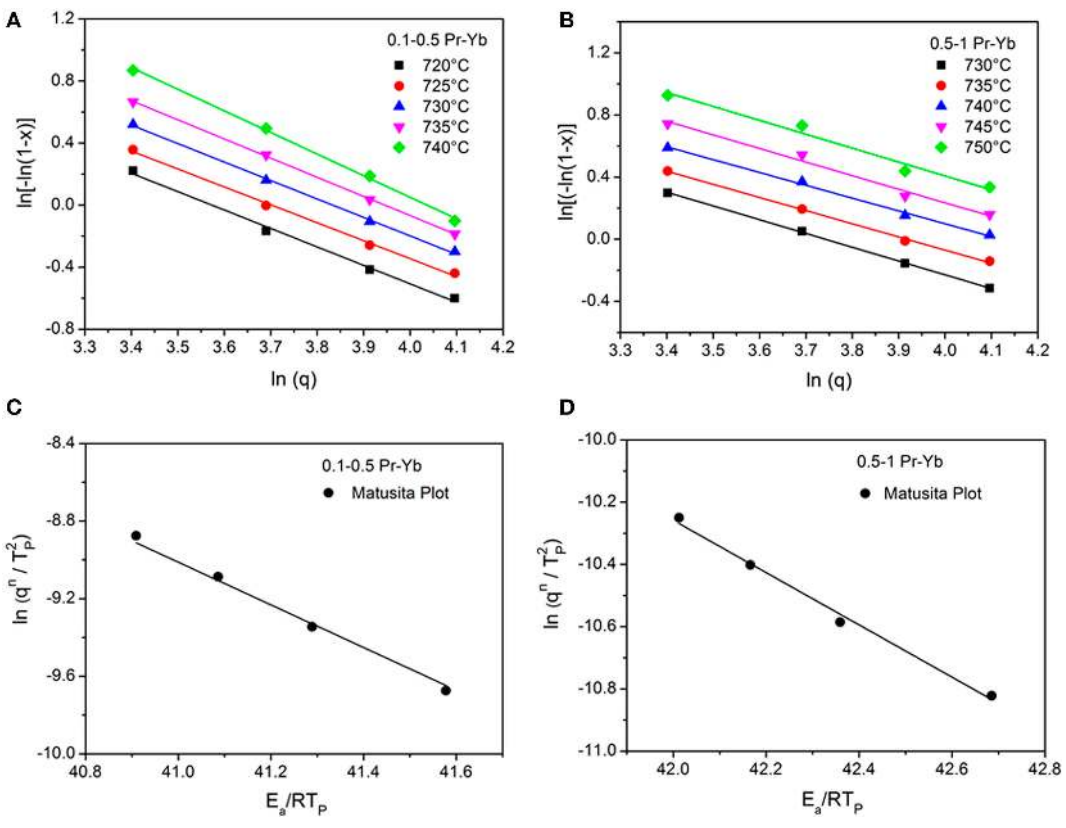


**FIGURE 2** | Ozawa plot for **(A)** 0.1–0.5 Pr–Yb and **(B)** 0.5–1 Pr–Yb doped glass. **(C)** Matusita plot for 0.1–0.5 Pr–Yb and **(D)** 0.5–1 Pr–Yb doped glass.

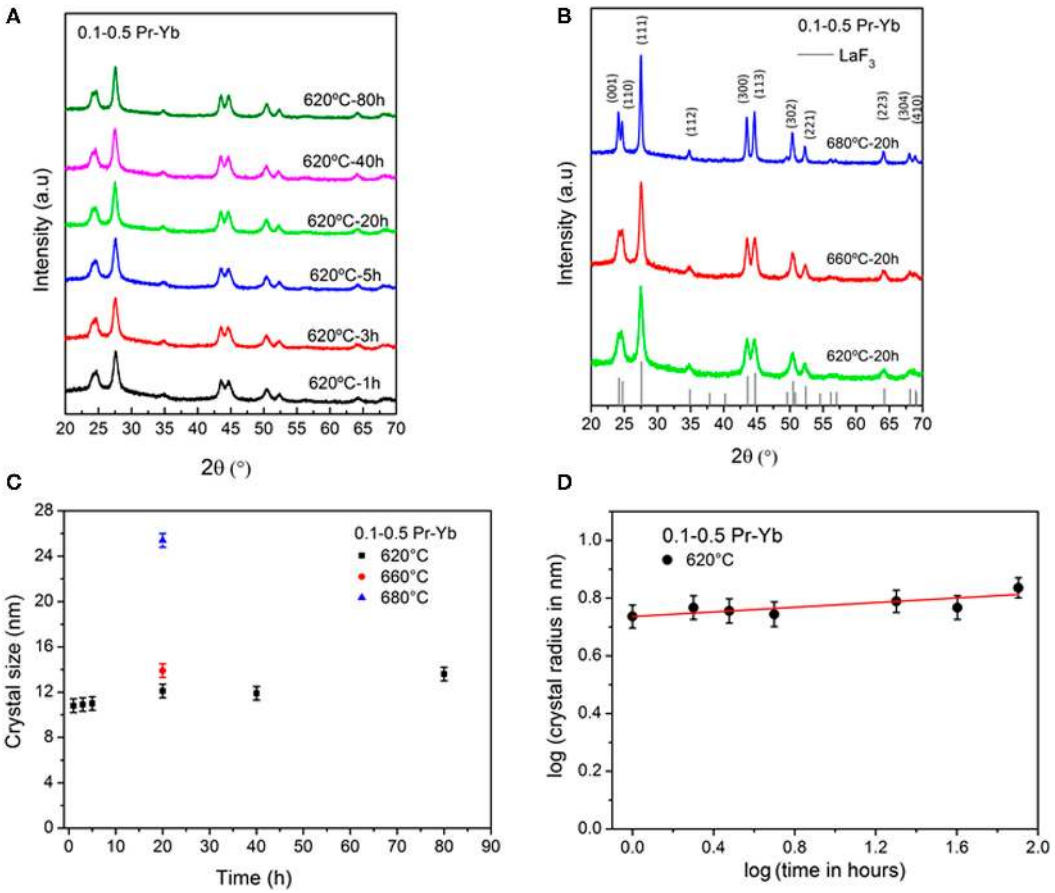


**FIGURE 3** | Diffractograms for glass-ceramics (GCs) 0.1–0.5 Pr–Yb treated at **(A)** 620°C for 1, 3, 5, 20, 40, and 80 h and at **(B)** 620, 660, and 680°C for 20 h. All diffractograms have been labeled by their Miller indices and the $LaF_3$ reference peaks are shown in the bottom. **(C)** Crystal size variation with the treatment time or temperature for GC 0.1–0.5 Pr–Yb treated at 620°C (square) during 1, 3, 5, 20, 40, 80 h, 660°C (circle) and 680°C (triangle) for 20 h. **(D)** Crystal growth *p* exponent for GCs treated at 620°C during 1, 3, 5, 20, 40, and 80 h.

Scherrer equation (Eq. 4), to take into account the instrumental broadening, applied to $LaF_3$ (111) peak ($2\theta \approx 27.5°$).

Crystal growth exponent $p$ has been estimated by Eq. 6. **Figure 3C** shows crystal size variation with treatment time, and **Figure 3D** shows the crystal growth exponent $p$ for GCs 0.1–0.5 Pr–Yb.

For GCs, 0.1–0.5 Pr–Yb crystals size at 620°C, shown in **Figure 3C**, is almost constant ≈12 nm for different treatment times, while treating the samples at different temperatures for the same time of 20 h, crystals size shows important changes. The increase of crystals size at higher temperature is indicated by the more intense diffraction peaks and by the narrowing of the peaks. At 660°C, crystals size is ≈14 nm and at 680°C ≈ 26 nm. As a consequence, for the heat treatment at 680°C, 20 h, the material partially lost its transparency due to quite bigger crystals. In fact, even though crystals are still quite small, the phase separation droplets containing several crystals inside have quite bigger sizes (as it will be shown in next section—Section "TEM"), ranging from an average value of 37 nm at 620°C up to ≈100 nm at 680°C. The GC starts to loose transparency at temperatures higher than 660°C. Moreover, temperatures higher than the glass softening temperature, ≈670°C, are not useful for practical purpose.

Glass-ceramics 0.5–1 Pr–Yb treated at 620°C, 1 h are almost amorphous and crystal size stabilizes to a constant value, around 11 nm, for treatments longer than 3 h. The onset of crystallization is delayed compared to GCs doped with 0.1–0.5 Pr–Yb, and this is associated with the higher activation energy (342 kJ/mol vs 329 kJ/mol). This is related to the nucleating effect of fluorides which promotes the production of smaller nuclei compared to what happens with lower fluoride content, according to which smaller nuclei should be favored. In fact, it is known that fluorine content in oxyfluoride glasses acts as a nucleating agent and suppresses crystal growth by increasing nuclei quantity (Chen et al., 2007; Bhattacharyya et al., 2009).

$Pr^{3+}$ singly doped samples showed very similar behavior and only $LaF_3$ crystals precipitate in the glass matrix, and the crystals size is similar to the one obtained for the co-doped samples.

The calculation of $p$ exponents was carried out using Eq. 6, starting from plots of crystals size for GCs treated at 620°C for 20 h. Data are plotted in **Figure 3D** for GCs 0.1–0.5 Pr–Yb. The crystal growth exponent at 620°C is $p = 0.040 \pm 0.005$, while for GCs 0.5–1 Pr–Yb the $p$ exponent is $p = 0.03 \pm 0.01$. The very small dependence of crystal growth on the time of heat treatment together with small values for crystal growth exponent $p$, indicates the presence of an inhibition phenomenon explained in detail in Bhattacharyya et al. (2009) and de Pablos-Martín et al. (2011, 2012). These previous studies showed that La and Si-enriched phase separation droplets are precipitated already during the preparation of the initial glass. Upon conversion of the glass into a nano-GCs by appropriate annealing, $LaF_3$ nano-crystals are formed within these droplets. Similar results have been obtained in this work as shown in Section "TEM."

## TEM

**Figure 4A** shows a TEM image of the 0.1–0.5 Pr–Yb glass. The starting glass presents phase separation with a narrow size distribution of the droplets between 15–40 nm and an average droplets size of 28 nm (**Figure 4B**). The majority of the droplets do not present any structure inside. However, in very few droplets, small crystalline domains of 5–7 nm in size have been also detected, but this incipient crystallinity in the base glass is not detectable by XRD. The chemical composition along 80 nm scanning line (**Figure 4C**) was measured by EDXS and represented in **Figure 4D**. The droplets are enriched in F, La, Pr and Yb, a clear evidence of RE incorporation inside the droplets. Furthermore, excess of Si and Al are relocated toward the periphery of the droplets, and the formation of a barrier enriched in glass formers prevent further crystal growth, during the crystallization process, due to the increase of viscosity.

**Figure 5A** shows an image of the GC 0.1–0.5 620°C, 20 h and bigger droplets, with average size ≈33 nm, were detected as compared to the untreated glass (**Figure 5B**). A feature of this glass system is the crystals formation inside the initial phase separation droplets, already enriched in crystals components in the as made glass. The size of the crystals inside each droplet is clearly observed in **Figure 5C**, and their size distribution is represented in **Figure 5D**. An average crystals size of 10 nm was obtained for this heat treatment, in agreement with the value obtained by XRD

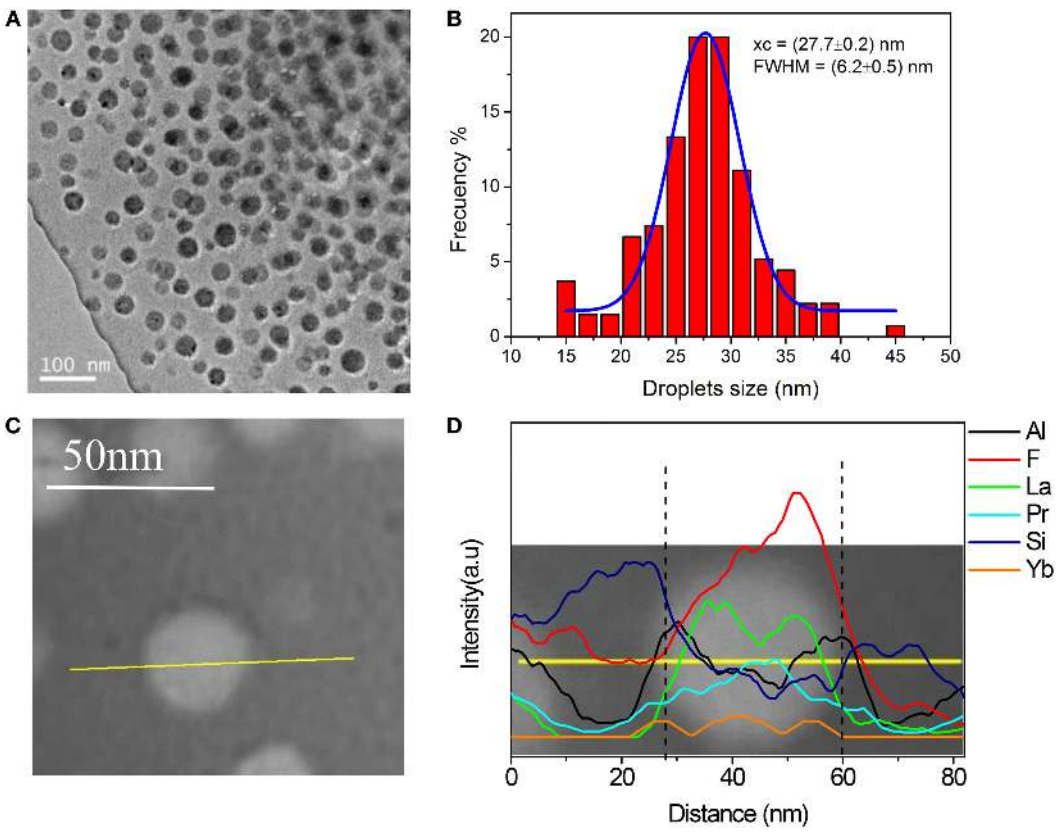


**FIGURE 4** | **(A)** TEM image of the 0.1–0.5 Pr–Yb glass showing phase separation droplets. **(B)** Droplet size distribution. **(C)** STEM image of the glass sample where the yellow line is the scanning line along which EDXS analysis was performed **(D)**.

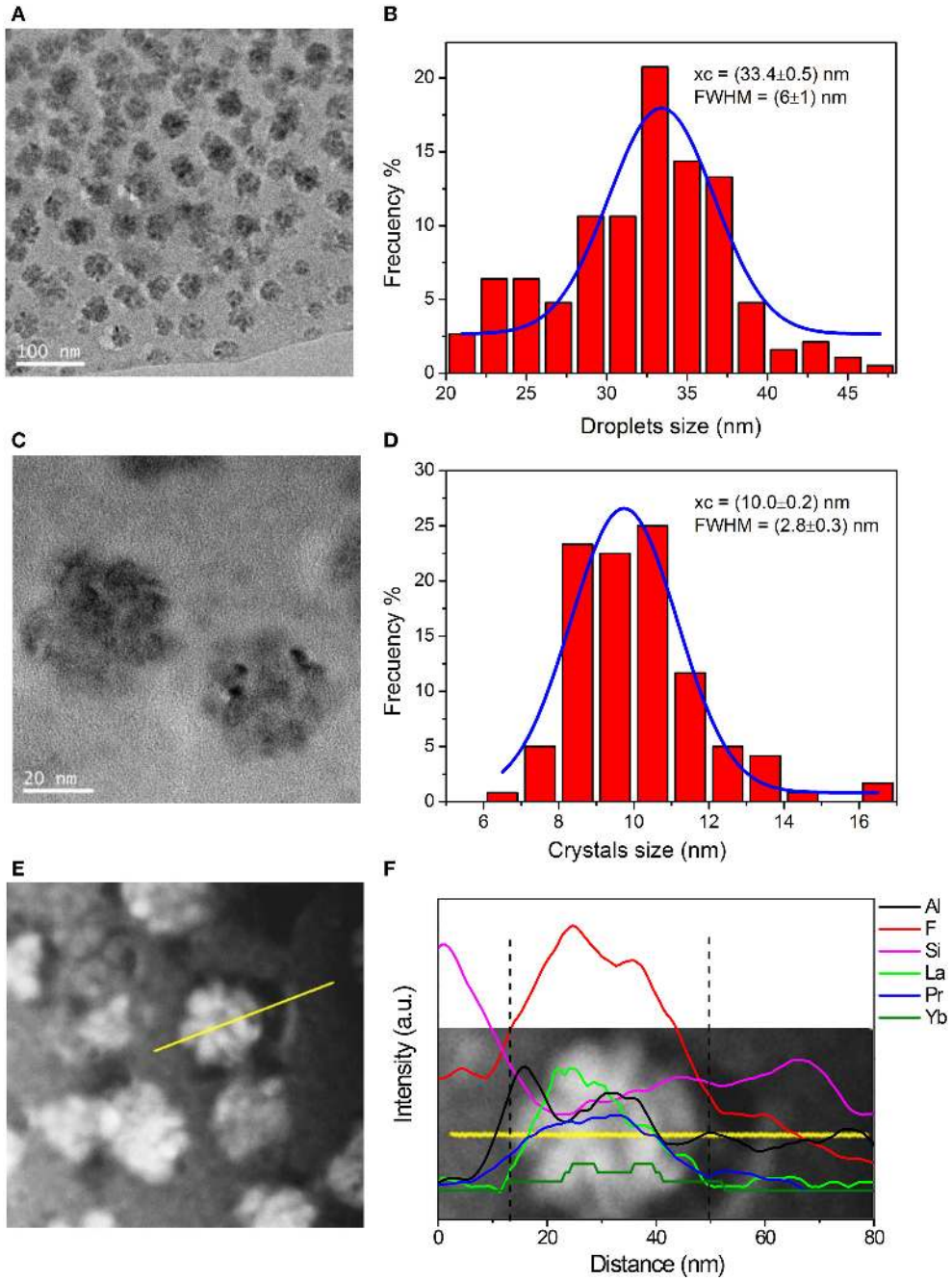


**FIGURE 5** | **(A)** TEM image of the glass-ceramic 0.1–0.5 Pr–Yb 620°C, 20 h and corresponding droplet size distribution **(B)**. **(C)** TEM image of two droplets and cystals size distribution inside the droplet **(D)**. **(E)** STEM image of the sample and EDXS analysis along the yellow line containing one droplet **(F)**.

measurements. **Figures 5E,F** show EDXS analysis of one single droplet. Al and Si are mostly confined in the interphase and tend to be smaller in correspondence of the maximum F, La, Pr, and Yb concentration, i.e., inside the droplet. Clear presence of RE ions inside the phase separation droplets and crystals is observed for glass and GCs. The detection of Yb is quite difficult, but its presence in the crystals is observed.

## Optical Properties

UV–VIS optical density for $Pr^{3+}$- and $Pr^{3+}$–$Yb^{3+}$-doped glasses and GCs are represented in **Figure 6**.

Glasses have lower absorbance compared to GCs that suffer Rayleigh scattering caused by density fluctuations due to the presence of nano-crystals inside the glass matrix. The strong UV absorption (Urbach tail) below 350 nm is due to electronic

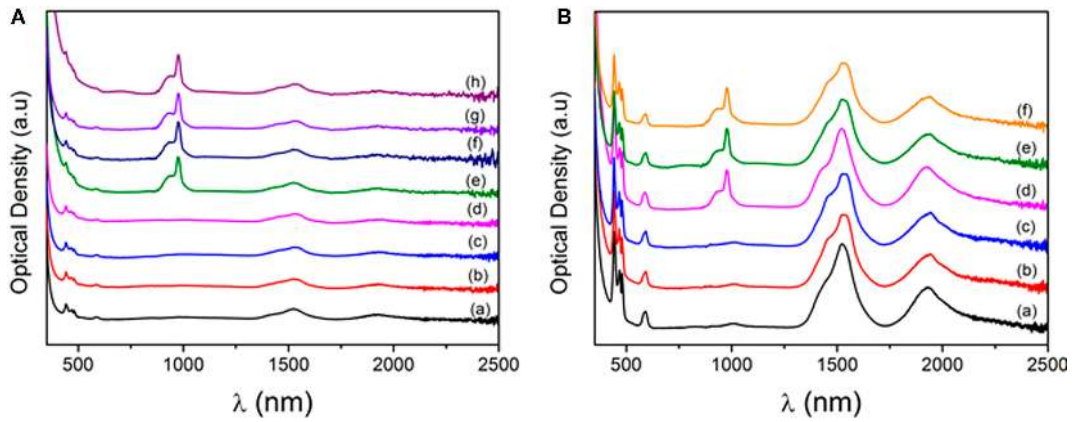


**FIGURE 6** | **(A)** Optical density for Glass 0.1 Pr (a), glass-ceramic (GC) 0.1 Pr 620°C, 20 h (b), GC 0.1 Pr 620°C, 40 h (c), GC 0.1 Pr 660°C, 20 h (d), Glass 0.1–0.5 Pr–Yb (e), GC 0.1–0.5 Pr–Yb 620°C, 20 h (f), GC 0.1–0.5 Pr–Yb 620°C, 40 h, and GC 0.1–0.5 Pr–Yb 660°C, 20 h (h). **(B)** Optical density for Glass 0.5 Pr (a), GC 0.5 Pr 620°C, 40 h (b), 0.5 Pr GC 660°C, 20 h (c), glass 0.5–1 Pr–Yb (d), GC 0.5–1 Pr–Yb 620°C, 40 h (e), and GC 0.5–1 Pr–Yb 660°C, 20 h (f).

transitions between the ligand (oxygen mainly) and the glass network former ion (silicon). In all materials the transitions between the 4f and 4f states corresponding to $Pr^{3+}$ and $Yb^{3+}$ ions are clearly visible. From the left, the following $Pr^{3+}$ transitions can be assigned: $^3H_0$–$^3P_{2,1,0}$ at 442, 466, and 480 nm, $^3H_4$–$^1D_2$ at 590 nm, $^3H_4$–$^3F_4$ at 1460 nm, $^3H_4$–$^3F_3$ at 1590, and $^3H_4$–$^3F_2$ at 1930 nm. The $Yb^{3+}$ transition $^2F_{7/2}$–$^2F_{5/2}$ is also observed at 980 nm. For 0.5 Pr and 0.5–1 Pr–Yb GCs (**Figure 6B**), a small underlying structure is observed for $Pr^{3+}$ absorption to the $^3F_3$ level, reflecting the different local field felt by $Pr^{3+}$ ions compared to glasses, a proof of $Pr^{3+}$ incorporation inside $LaF_3$ crystals that causes a narrowing of the band and the Stark components can be appreciated. However, clearer evidence of $RE^{3+}$ ions inside $LaF_3$ crystals appears in the PL spectra.

PL spectra for $Pr^{3+}$ doped and $Pr^{3+}$–$Yb^{3+}$ co-doped glasses and GCs are given in **Figure 7**. Excitation has been provided by an InGaN LED centered at 435 nm and $Pr^{3+}$ ions have been excited to the $^3P_2$ level. By non-radiative decay, the $^3P_0$ level is populated and $Pr^{3+}$ radiative emissions from this level to the three excited states $^3H_{4,5,6}$ and $^3F_{2,3,4}$ are clearly visible in the range 450–750 nm.

For samples singly doped with $Pr^{3+}$, the emission at 1.05 μm corresponding to the transition from $^1D_2$–$^3F_{3,4}$ levels is observed and the emission at 600 nm corresponding to the $^1D_2$–$^3H_4$ transition, in both doped and co-doped samples, overlaps with the $^3P_0$–$^3H_6$ emission band. The population of $^1D_2$ level is due to multi-phonon relaxation from the $^3P_0$ level, and this contribution is stronger in glass than in GCs, meaning the incorporation of $Pr^{3+}$ ions inside $LaF_3$ crystals, where phonons are much smaller.

However, in co-doped samples, the $^3P_0$ level is also quenched by the presence of $Yb^{3+}$ ions, producing a DC signal in the range 950–1150 nm, as a consequence of an ET process. The $Pr^{3+}$ transition $^1G_4$–$^3H_5$ at 1.3 μm is not observed in any samples, glass or GCs. Moreover, the $^3P_0$–$^1G_4$ transition at 950 is not osberved either.

For all samples, a more evident distinction in the $Pr^{3+}$ emission between glass and GCs is observed. Again, co-doped glasses present the lowest $Yb^{3+}$ DC signal at 976 nm while the $Pr^{3+}$ transition $^3P_0$–$^3H_6$ gets smaller passing from glass to GCs. Glass does not show sharp Stark splitting while a clear splitting of the $^3H_{5,6}$ and $^3F_4$ is visible in the GCs, a convincing proof that $Pr^{3+}$ ions are incorporated into $LaF_3$ crystals. However, $Yb^{3+}$ ions should be incorporated in $LaF_3$ crystals as well. In fact, a difference in the local environment between $Pr^{3+}$ and $Yb^{3+}$ does not seem favorable for ET processes. Additionally, DC emission gets stronger in GCs.

Xu et al. (2011) studied a 0.5–0.5 Pr–Yb doped oxyfluoride GCs containing $LaF_3$ crystals and found that the visible emission increases more than NIR emission passing from glass to GCs. Moreover, NIR emission of $Yb^{3+}$ ions did not increase monotonously with the heat treatment temperature or time. These results are in contradiction with ours. They concluded that $Yb^{3+}$ ions are not favored to be incorporated inside $LaF_3$ crystals, while we observed incorporation. TEM images (**Figure 5**), and particularly the elemental analysis with 1 nm resolution, showed an enrichment of $Yb^{3+}$ inside the droplets, while no significant $Yb^{3+}$ concentration was detected in the glass matrix.

While for 0.1–0.5 Pr–Yb doped samples the effect of the increase of temperature seems comparable to the increase of heat treatment time, for 0.5–1 Pr–Yb doped materials the increase of temperature produces the most evident improvement of $Yb^{3+}$ DC emission at 976 nm. This may be explained considering that a doping with 0.1–0.5 Pr–Yb produces a lower nuclei density, but bigger crystals are still possible by rising the annealing temperature (**Figure 3C**). In particular, bigger crystals can host more $RE^{3+}$ ions and a heat treatment at 620°C, 40 h thus produces an improvement of DC signal.

For 0.5–1 Pr–Yb, due to the quite higher fluoride content into the initial melt, the as made glass has a higher nuclei density thanks to the nucleating action of fluorine. The smaller initial

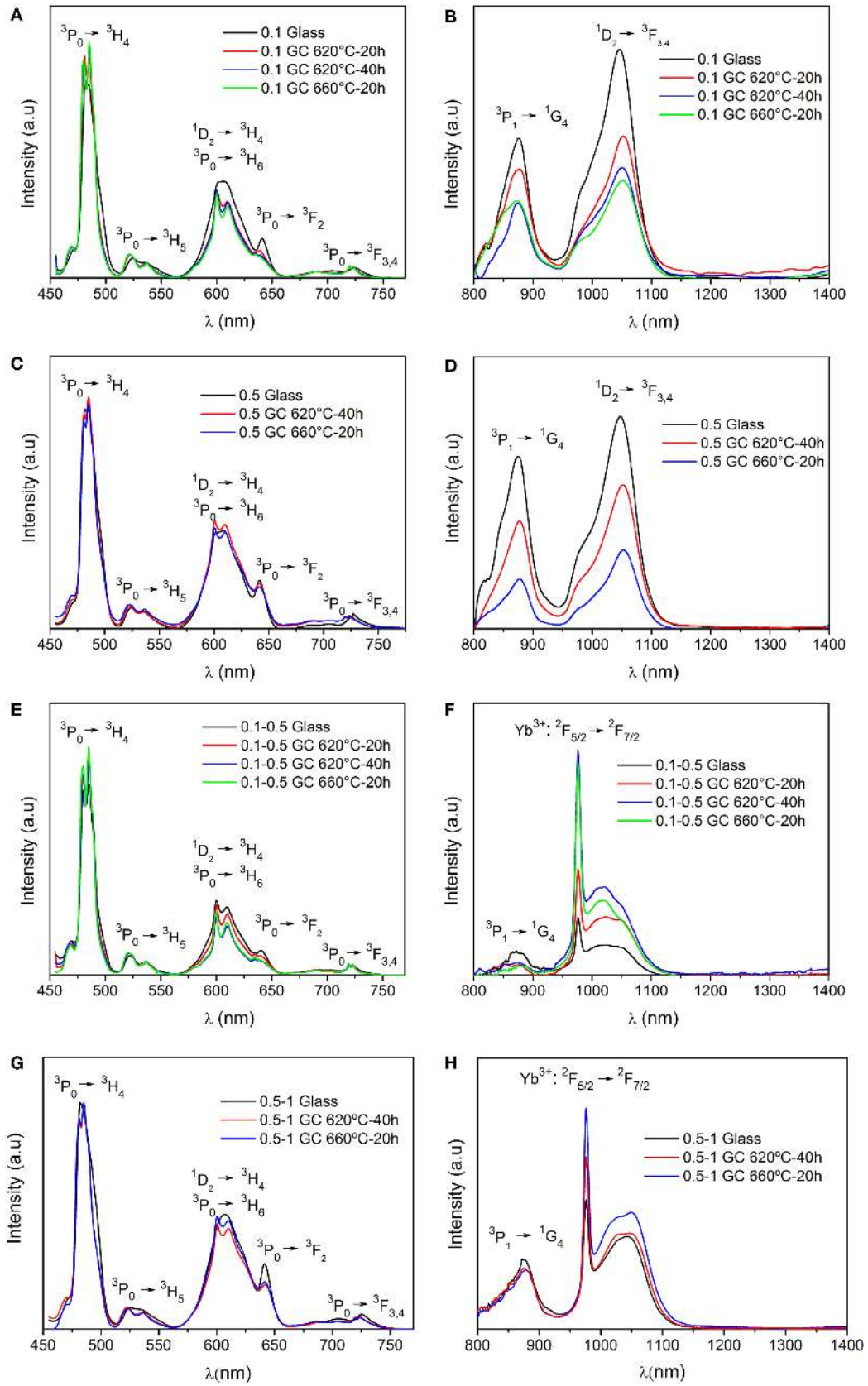


**FIGURE 7** | PL emission spectra for **(A,B)** 0.1 Pr, **(C,D)** 0.5 Pr, **(E,F)** 0.1–0.5 Pr–Yb, **(G,H)** 0.5–1 Pr–Yb doped samples. Excitation is at 435 nm.

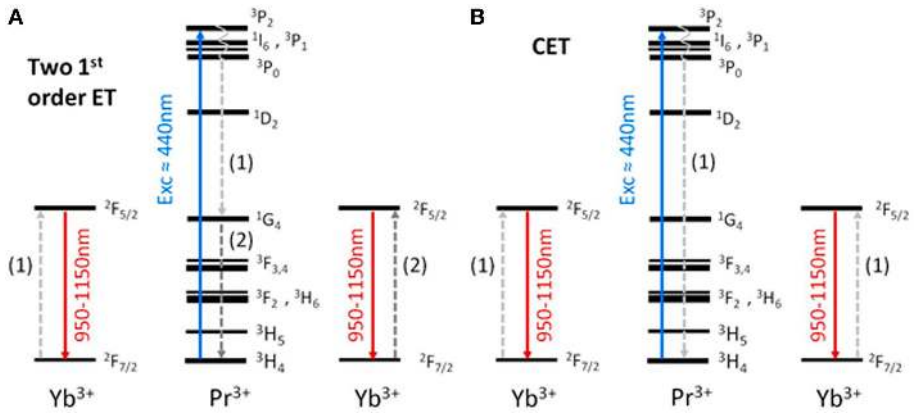


**FIGURE 8** | **(A)** Two first order energy transfer (ET) processes, the first being a cross relaxation. **(B)** Cooperative energy transfer between one $Pr^{3+}$ and two $Yb^{3+}$ ions.

nuclei make it more difficult to produce bigger crystals, due to the reduction of the effective cross-section to capture other crystal forming ions and to the presence of a diffusion barrier of higher viscosity around $LaF_3$ crystals that is formed earlier and which is expected to be thicker. In addition, in a glass doped with more $RE^{3+}$ ions, viscosity increases compared to un-doped glass (or to a less doped glass), at the temperatures of nano-glass ceramic formation ($T_g$ + 20–80°C) (de Pablos-Martín et al., 2013). As a consequence, $RE^{3+}$ ions diffusion inside crystals can require longer times, and therefore, the best improvement is obtained by rising the temperature until a decrease of viscosity starts to allow more $RE^{3+}$ ions diffusion inside the $LaF_3$ crystals but avoiding the growth of nanocrystals above 20 nm.

As suggested by van Wijngaarden et al. (2010), the cross relaxation scheme, **Figure 8A**, is the most common scheme for Pr–Yb DC. The two step ET process firstly allows $Yb^{3+}$ ions excitation to the $^2F_{5/2}$, and then $Pr^{3+}$ ions from the $^1G_4$ level transfer energy to $Yb^{3+}$ ions.

Xiang et al. (2014) found that, increasing $Yb^{3+}$ concentration to 10 mol%, cooperative energy transfer (CET) process, **Figure 8B**, becomes increasingly important and for very high concentration as 20 mol% CET process is the main ET process.

In this study, the absence of the emission at 1.3 μm ($^1G_4$–$^3H_5$) from $Pr^{3+}$ ions indicates that $^1G_4$ level is not populated or that this level is highly quenched in glass as well as in GCs. Considering that even for glass samples doped with only 0.1 mol% of $Pr^{3+}$ this emission is not observed, we are tempted to affirm that this transition hardly occurs in our samples. Furthermore, the $^3P_0$–$^1G_4$ transition at 950 nm is not observed in any sample and this is in agreement with the absence of population of the $^1G_4$ level and finally, it could be a proof of the fact that the CET from the $Pr^{3+}$ $^3P_0$ can be relevant for co-doped samples. Hence, it is possible to conclude that the ET between $Pr^{3+}$ to $Yb^{3+}$ ($^2F_{7/2}$–$^2F_{5/2}$) is improved in GCs respect to glass and CET could be quite relevant.

As suggested by Gao and Wondraczek (2013), the ET from the $^1G_4$ level of $Pr^{3+}$ to the $^2F_{5/2}$ level of $Yb^{3+}$ is rather unlikely because the $^1G_4$ level is almost 200 $cm^{-1}$ lower than the $Yb^{3+}$ $^2F_{5/2}$ level and an opposite back ET, from the $Yb^{3+}$ $^2F_{5/2}$ to the $Pr^{3+}$ $^1G_4$ level, should be favored. Considering that the ET from $^1G_4$ of $Pr^{3+}$ to the $^2F_{5/2}$ of $Yb^{3+}$ is not observed in our measurements, the back ET from $Yb^{3+}$ to $Pr^{3+}$ ions was also studied by direct excitation of $Yb^{3+}$ ions with a laser fiber at 976 nm. The corresponding PL measurements for GCs 0.1–0.5 Pr–Yb GC are given in **Figure 9**. The same results have been obtained for the GCs 0.5–1 Pr–Yb.

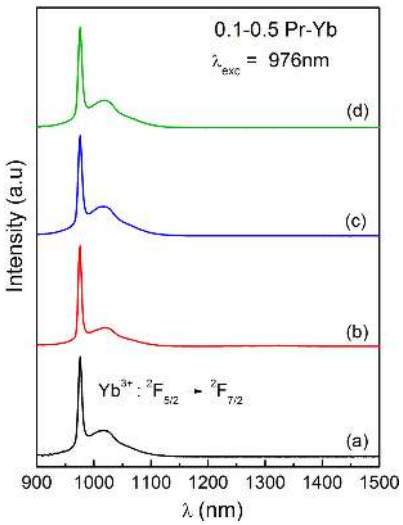


**FIGURE 9** | PL spectra upon Yb3+ direct excitation at 976 nm for the glass (a), glass-ceramics (GC) 620°C, 20 h (b), GC 620°C, 40 h (c), and GC 660°C, 20 h (d) for the 0.1–0.5 Pr–Yb composition.

As clearly observed, no $Pr^{3+}$ emission is present for direct excitation of $Yb^{3+}$ at 976 nm, meaning the absence of a back ET mechanism. Therefore, the first order ET from $^1G_4$ of $Pr^{3+}$ to $^2F_{5/2}$ of $Yb^{3+}$ is quite unlikely.

**Figure 10** shows $Pr^{3+}$ lifetime at 610 nm ($^3P_0$–$^3H_6$) for 0.1–0.5 Pr–Yb and 0.5–1 Pr–Yb co-doped samples, respectively. Lifetimes have been calculated by best fit and in all cases a bi-exponential fit has been necessary. Fast decays correspond to ET between neighbor ions while longer lifetimes give indication

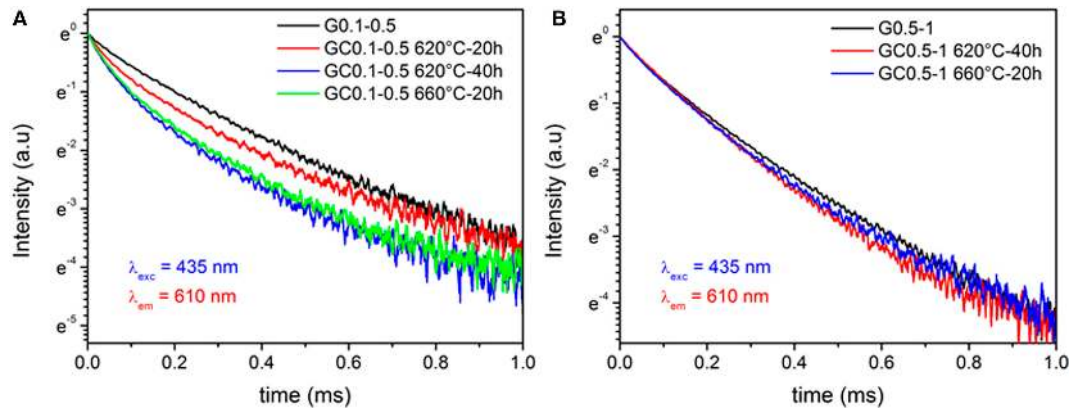


**FIGURE 10** | $Pr^{3+}$:$^3P_0$–$^3H_6$ transition lifetime at 610 nm upon 435 nm excitation, for **(A)** 0.1–0.5 Pr–Yb and **(B)** 0.5–1 Pr–Yb co-doped samples.

**TABLE 2 | $Pr^{3+}$ lifetime at 610 nm for co-doped and $Pr^{3+}$ singly doped (in parenthesis) glasses and glass-ceramics (GCs) with the corresponding energy transfer efficiency (ETE) and quantum efficiency (QE).**

| Sample | Lifetime (μs) | ETE (%) | QE (%) |
|---|---|---|---|
| G 0.1–0.5 | 240 (269) | 11 | 111 |
| GC 0.1–0.5 620°C, 20 h | 147 (271) | 46 | 146 |
| GC 0.1–0.5 620°C, 40 h | 123 (297) | 59 | 159 |
| GC 0.1–0.5 660°C, 20 h | 127 (290) | 56 | 156 |
| G 0.5–1 | 214 (235) | 9 | 109 |
| GC 0.5–1 620°C, 40 h | 165 (298) | 44 | 144 |
| GC 0.5–1 660°C, 20 h | 150 (277) | 46 | 146 |

about radiative emission lifetime, although there can be also not negligible contributions from ET over long distances (Katayama and Tanabe, 2013). Lifetime uncertainty is ≈ 5%. $Pr^{3+}$ emission in GCs has a more evident non-exponential profile. $Pr^{3+}$ decays in co-doped samples is faster than glass, and this is a further proof of a more efficient ET mechanism between $Pr^{3+}$ and $Yb^{3+}$ ions. For $Pr^{3+}$ singly doped samples, lifetime increases passing from glass to GCs and their values are summarized in **Table 2**.

ETE and QE of all co-doped samples have been calculated using Eqs 8 and 9. An estimation of the highest theoretical QE was obtained setting $\eta_{Pr}$ and $\eta_{Yb}$ in Eq. 9 equal to 1. The values are summarized in **Table 2**. ETE is quite smaller for glass than for GCs and for 0.1–0.5 Pr–Yb composition it is 11% for glass and almost 60% for GC 620°C, 40 h and the highest QE is 159%. For 0.5–1 Pr–Yb, the highest ETE value, obtained for GC 660°C, 20 h, is 46% and the highest QE is 146%. Therefore, the best results in terms of ETE and QE are obtained for the 0.1–0.5 Pr–Yb GC 620°C, 40 h, and this could be explained considering the higher ratio between $Pr^{3+}$ and $Yb^{3+}$ ions that should favor a more uniform $Yb^{3+}$ distribution around $Pr^{3+}$ increasing the probability of DC emission.

**Figure 11** shows $Yb^{3+}$ emission at 976 nm for both co-doped compositions. Near single exponential decay are observed for GCs samples, while non-radiative relaxation channels are more important for glasses. GCs lifetimes increase as compared to glasses and this is a further proof of $Yb^{3+}$ ions inside $LaF_3$ crystals. All $Yb^{3+}$ lifetimes are summarized in **Table 3**.

## CONCLUSION

Nano oxyfluoride GCs doped with 0.1 and 0.5 Pr and co-doped with 0.1–0.5 Pr–Yb and 0.5–1 Pr–Yb have been prepared with $LaF_3$ as only crystal phase. In all the cases, glasses and GCs treated at 620 and 660°C are perfectly transparent, due to the small crystal size (12–14 nm).

Crystallization kinetics showed that the crystal growth of $LaF_3$ starts from a constant number of nuclei already present in the as made glass and the process is controlled by diffusion. In particular, by increasing dopants concentration, the nuclei density increases but nuclei size gets smaller. Likewise, the increase of $T_g$ and $T_x$ for higher dopants concentrations causes a delay in the crystallization onset and limits $RE^{3+}$ ions diffusion due to higher viscosity.

Down-conversion emission of $Yb^{3+}$ was observed in the range 950–1,150 nm upon $Pr^{3+}$ excitation at 440 nm, and CET from the $^3P_0$ level of $Pr^{3+}$ could play relevant role in the ET process from $Pr^{3+}$ to $Yb^{3+}$.

$Pr^{3+}$ and $Yb^{3+}$ ions get incorporated inside $LaF_3$ crystals in GCs samples. This fact is strongly supported by the more evident Stark splitting of $Pr^{3+}$ emission spectra passing from glass to GCs, by the $Pr^{3+}$ lifetime decrease in GCs suggesting that a better ET occurs and by $Yb^{3+}$ lifetime increase in GCs indicating a decrease of non-radiative processes compared to glasses.

Glass-ceramics samples show better DC emission in the range 950–1150 nm compared to glasses and by a proper heat treatment it is possible to find the best combination to enhance $Yb^{3+}$ DC and suppress unwanted $Pr^{3+}$ emission. The highest ETE and QE were 59 and 159%, respectively, for GC 0.1–0.5 Pr–Yb 620°C, 40 h.

The results here described encourage continuing with further analysis of these materials as DC materials. In particular, different $RE^{3+}$ ions concentration combinations should be tested. The DC emission by $Yb^{3+}$ ions show the possibility of using this glass system in Photonics, even though further studies, regarding $RE^{3+}$ ions concentrations, materials thickness, etc., should be performed to optimize the best DC signal and the application of these materials.

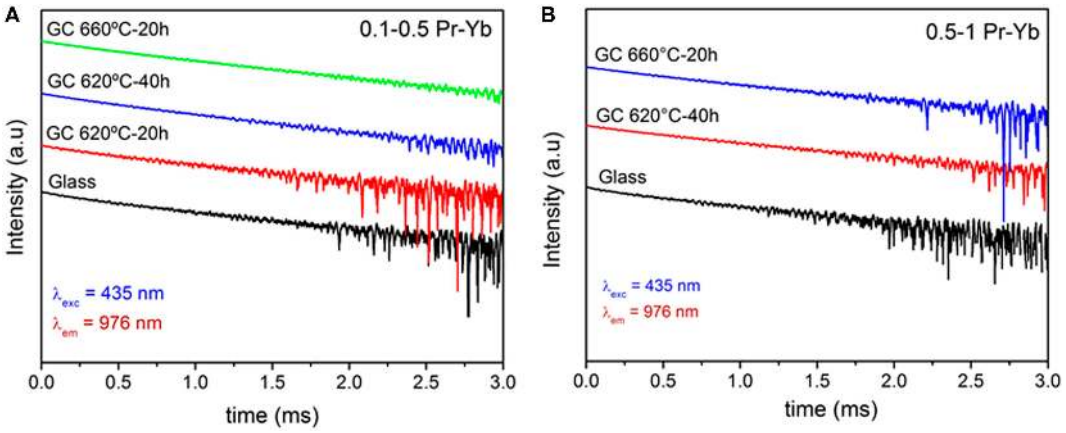


**FIGURE 11** | $Yb^{3+}$:$^2F_{5/2}$–$^2F_{7/2}$ transition lifetime at 976 nm upon 435 nm excitation, for **(A)** 0.1–0.5 Pr–Yb and **(B)** 0.5–1 Pr–Yb co-doped samples.

**TABLE 3 | $Yb^{3+}$: $^2F_{5/2}$–$^2F_{7/2}$ lifetime for all co-doped samples.**

| Sample | Lifetime (μs) |
|---|---|
| G 0.1–0.5 | 640 |
| GC 0.1–0.5 620°C, 20 h | 750 |
| GC 0.1–0.5 620°C, 40 h | 758 |
| GC 0.1–0.5 660°C, 20 h | 756 |
| G 0.5–1 | 630 |
| GC 0.5–1 620°C, 40 h | 700 |
| GC 0.5–1 660°C, 20 h | 705 |

## AUTHOR CONTRIBUTIONS

GG prepared the materials and studied their structural properties. He also measured lifetimes with SP. He contributed to the discussion of results and writing of the paper. AC contributed to the PL measurements. SP contributed to the management of the experiment and to the PL and lifetime measurements. LP performed HR-TEM characterization and analysis. AD and MP contributed to the structure and planning of the work, management of the experiments, work supervision and discussion, and writing of the paper.

## ACKNOWLEDGMENTS

The authors would like to thank Juan Vargas (technician at ICV-CSIC) for samples preparation.

## FUNDING

Financial support of the Spanish National Project MAT2013-48246-C2-1-P. GG wishes to acknowledge a grant given by the Tuscany region "Progetto Giovani Si" (Italy). AC wishes to acknowledge the financial support of the Ministero dell'Istruzione, dell'Università e della Ricerca (MIUR) through the Centro Fermi project "Premiale 2012 – Fisica e strumentazione per la salute dell'uomo."

## REFERENCES

Abrams, Z. R., Niv, A., and Zhang, X. (2011). Solar energy enhancement using down-converting particles: a rigorous approach. *J. Appl. Phys.* 109, 114905–114909. doi:10.1063/1.3592297

Bhattacharyya, S., Höche, T., Hemono, N., Pascual, M. J., and van Aken, P. A. (2009). Nano-crystallization in $LaF_3$-$Na_2O$-$Al_2O$-$SiO_2$ glass. *J. Cryst. Growth* 311, 4350–4355. doi:10.1016/j.jcrysgro.2009.07.027

Chen, D., Wang, Y., Yu, Y., Huang, P., and Weng, F. (2008). Near-infrared quantum cutting in transparent nanostructured glass-ceramics. *Opt. Lett.* 33, 1884–1886. doi:10.1364/OL.33.001884

Chen, D., Wang, Y., Yu, Y., and Ma, E. (2007). Influence of $Yb^{3+}$ content on microstructure and fluores-cence of oxyfluoride glass-ceramics containing $LaF_3$ nano-crystals. *Mater. Chem. Phys.* 101, 464–469. doi:10.1016/j.matchemphys.2006.08.005

Chen, Q. J., Zhang, W. J., Huang, X. Y., Dong, G. P., Peng, M. Y., and Zhang, Q. Y. (2012). Efficient down- and up-conversion of $Pr^{3+}$-$Yb^{3+}$ co-doped transparent oxyfluoride glass-ceramics. *J. Alloys Compd.* 513, 139–144. doi:10.1016/j.jallcom.2011.10.007

de Pablos-Martín, A., Durán, A., and Pascual, M. J. (2012). Nanocrystallisation in oxyfluoride systems: mechanisms of crystallisation and photonic properties. *Int. Mater. Rev.* 57, 165–186. doi:10.1179/1743280411Y.0000000004

de Pablos-Martín, A., Hemono, N., Mather, G. C., Bhattacharyya, S., Höche, T., Bornhöft, H., et al. (2011). Crystallization kinetics of $LaF_3$ nanocrystals in an oxyfluoride glass. *J. Am. Ceram. Soc.* 94, 2420–2428. doi:10.1111/j.1551-2916.2011.04547.x

de Pablos-Martín, A., Ristic, D., Bhattacharyya, S., Höche, T., Mather, G. C., Ramırez, M. O., et al. (2013). Effects of $Tm^{3+}$ additions on the crystallization of $LaF_3$ nanocrystals in oxyfluoride glasses: optical characterization and up-conversion. *J. Am. Ceram. Soc.* 96, 447–457. doi:10.1111/jace.12120

Deng, K., Wei, X., Wang, X., Chen, Y., and Yin, M. (2011). Near-infrared quantum cutting via resonant energy transfer from $Pr^{3+}$ to $Yb^{3+}$ in $LaF_3$. *Appl. Phys. B* 102, 555–558. doi:10.1007/s00340-011-4413-7

Donald, I. W. (2004). Crystallisation kinetics of a lithium zinc silicate glass studied by DTA and DSC. *J. Non Cryst. Solid* 345-346, 120–126. doi:10.1016/j.jnoncrysol.2004.08.007

Gao, G., and Wondraczek, L. (2013). Near-infrared down-conversion in $Pr^{3+}$/$Yb^{3+}$ co-doped boro-aluminosilicate glasses and $LaBO_3$ glass ceramics. *Opt. Mater. Express* 3, 633–644. doi:10.1364/OME.3.000633

Hemono, N., Pierre, G., Muñoz, F., de Pablos-Martín, A., Pascual, M. J., and Durán, A. (2009). Processing of transparent glass-ceramics by nano-crystallisation of $LaF_3$. *J. Eur. Ceram. Soc.* 29, 2915–2920. doi:10.1016/j.jeurceramsoc.2009.05.013

Huang, X., Han, S., Huang, W., and Liu, X. (2013). Enhancing solar cell efficiency: the search for luminescent materials as spectral converters. *Chem. Soc. Rev.* 42, 173–201. doi:10.1039/c2cs35288e

Katayama, Y., and Tanabe, S. (2010a). Near infrared down-conversion in $Pr^{3+}$–$Yb^{3+}$ codoped oxyfluoride glass ceramics. *Opt. Mater.* 33, 176–179. doi:10.1016/j.optmat.2010.07.016

Katayama, Y., and Tanabe, S. (2010b). Spectroscopy and 1 μm luminescence by visible quantum cutting in Pr3+-Yb3+ codoped glass. *Materials* 3, 2405–2411. doi:10.3390/ma3042405

Katayama, Y., and Tanabe, S. (2013). Mechanism of quantum cutting in $Pr^{3+}$–$Yb^{3+}$ codoped oxyfluoride glass ceramics. *J. Lumin.* 134, 825–829. doi:10.1016/j.jlumin.2012.06.042

Kissinger, H. E. (1956). Variation of peak temperature with heating rate in differential thermal analysis. *J. Res. Nat. Bur. Stand.* 57, 217–221. doi:10.6028/jres.057.026

Lakshminarayana, G., and Qiu, J. (2009). Near-infrared quantum cutting in $RE^{3+}/Yb^{3+}$ (RE = Pr, Tb, and Tm): $GeO_2$–$B_2O_3$–ZnO–$LaF_3$ glasses via down-conversion. *J. Alloys Compd.* 481, 582–589. doi:10.1016/j.jallcom.2009.03.034

Matusita, K., and Sakka, S. (1980). Kinetic study on crystallization of glass by differential thermal analysis – criterion on application of kissinger plot. *J. Non Cryst. Solid* 38, 741–746. doi:10.1016/0022-3093(80)90525-6

Ozawa, T. (1970). Kinetic analysis of derivative curves in thermal analysis. *J. Therm. Anal.* 2, 301–324. doi:10.1007/BF01911411

Richards, B. S. (2006). Luminescent layers for enhanced silicon solar cell performance: down-conversion. *Sol. Energy Mater. Sol. Cells* 90, 1189–1207. doi:10.1016/j.solmat.2005.07.001

Trupe, T., Green, M. A., and Wurfel, P. (2002). Improving solar cell efficiencies by down-conversion of high energy photons. *J. Appl. Phys.* 92, 1668–1674. doi:10.1063/1.1505677

van der Ende, B. M., Aarts, L., and Meijerink, A. (2009). Near-infrared quantum cutting for photovoltaics. *Adv. Mater.* 21, 3073–3077. doi:10.1002/adma.200802220

van Wijngaarden, J. T., Scheidelaar, S., Vlugt, T. J. H., Reid, M. F., and Meijerink, A. (2010). Energy transfer mechanism for down-conversion in the (Pr3+, Yb3+) Couple. *Phys. Rev. B* 81, 155112–155116. doi:10.1103/PhysRevB.81.155112

Xiang, G., Zhang, J., Hao, Z., Zhang, X., Pan, G., Luo, Y., et al. (2014). The energy transfer mechanism in $Pr^{3+}$ and $Yb^{3+}$ codoped β-$NaLuF_4$ nanocrystals. *Phys. Chem. Chem. Phys.* 16, 9289–9293. doi:10.1039/C4CP01184H

Xu, Y., Zhang, X., Dai, S., Fan, B., Ma, H., Adam, J.-L., et al. (2011). Efficient near-infrared down-conversion in Pr3+-Yb3+ codoped glasses and glass ceramics containing LaF3 nanocrystals. *J. Phys. Chem. C* 115, 13056–13062. doi:10.1021/jp201503v

Zhou, J., Tenga, Y., Ye, S., Linc, G., and Qiu, J. (2012). A discussion on spectral modification from visible to near-infrared based on energy transfer for silicon solar cells. *Opt. Mater.* 34, 901–905. doi:10.1016/j.optmat.2011.12.002

**Conflict of Interest Statement:** The authors declare that the research was conducted in the absence of any commercial or financial relationships that could be construed as a potential conflict of interest.